Soil Dynamics and Earthquake Engineering 115 (2018) 41–54

Contents lists available at ScienceDirect

Soil Dynamics and Earthquake Engineering

journal homepage: www.elsevier.com/locate/soildyn

Parametric models for 3D topographic amplification of ground motions considering subsurface soils

Gang Wang[a], Chunyang Du[a], Duruo Huang[a,b,*], Feng Jin[b], Raymond C.H. Koo[c], Julian S.H. Kwan[c]

[a] Department of Civil and Environmental Engineering, The Hong Kong University of Science and Technology, Hong Kong SAR
[b] Department of Hydraulic Engineering, Tsinghua University, Beijing, China
[c] Geotechnical Engineering Office, Civil Engineering and Development Department, Hong Kong SAR

ARTICLE INFO

Keywords:
ground-motion
numerical
NumericalumericalPredictionTopography-soil interactionnumericalTopographic amplification
Topography-soil interaction
Spectral element simulation
Prediction equation

ABSTRACT

Amplification of seismic waves due to surface topography and subsurface soils has often been observed to cause intensive damage in past earthquakes. Due to its complexity, topographic amplification has not yet been considered in most seismic design codes. In this study, we simulate ground-motion amplification based on 3D Spectral Element Method, using Hong Kong Island as a local testbed site. The analyses revealed that topographic amplification of ground motions is frequency-dependent. If the site is made of homogenous rock, the amplification factor is best correlated with the curvature smoothed over a characteristic length equal to half of the wavelength in rock. Amplification of high frequency wave is correlated with small-scale features, and amplification of long-period waves is correlated with large-scale features in horizontal dimension. The maximum topography amplification generally ranges from 1.6 to 2.0 on the protruded areas. When a low-velocity subsurface soil layer is considered, the topographic amplification pattern is significantly influenced by the thickness of the soil layer, as wavelength in soil is relatively short. The characteristic length reduces as soil thickness increases, and the amplification pattern becomes closely correlated to smaller-scale topographic features as well as slope angles. Results also show that the effect of material damping can be decoupled from the topographic effects and modeled using a theoretical attenuation factor. The study proposed parametric models to predict 3D topographic amplification using simple proxies considering subsurface soils, material damping and input wave frequencies, which gives accurate results with a standard deviation of residuals within 0.1–0.15.

1. Introduction

Amplification of seismic waves due to surface topography has often been observed as one of the major causes of intensive damage in past earthquakes. Due to focusing or defocusing of seismic waves, ground motions are usually amplified at convex features such as ridges and hill tops, and deamplified at concave features such as canyons and valleys (e.g. [1]). During the 1994 Northridge earthquake, a high peak ground acceleration (PGA) of 1.8 g was recorded at the Tarzana hill station [2]. A PGA as high as 1.25 g at the Pacoima Dam station caused damage to the abutment in the 1971 San Fernando earthquake [3]. These examples demonstrate that topography amplification is important for seismic design of buildings, retaining structures, pile foundations etc. on top of these features. Considering topographic amplification is particularly important for seismic design in mountainous regions like Hong Kong.

Due to its complexity, topographic amplification has not yet been considered in most seismic design codes, with only a few exceptions such as the Eurocode 8, the 1995 France seismic code and the 2010 Chinese seismic code [4]. Eurocode 8 [5] prescribes a topographic amplification factor that is frequency-independent using a simplified classification of ridge geometry and slope angle [6]. Based on field observations and 2D numerical analyses, the recent Chinese code specifies a topographic amplification factor of 1.1–1.6 according to the thickness of soils/rocks in the protruded area and average slope angles of the terrain. Although researches have indicated the topographic amplification is frequency-dependent, the code specifications are still frequency-independent. With the advancement of computational technology, numerical simulation of wave propagation becomes increasingly important to advance our understanding of the topographic amplification of ground motions, together with considerable efforts in field instrumentation and case-history studies. In the past, most of numerical analyses, and thus some existing seismic design codes, were based on analysis of simple 2D topography with uniformly distributed soils (e.g.,

* Corresponding author.
E-mail addresses: gwang@ust.hk (G. Wang), huangdr@ust.hk (D. Huang), jinfeng@tsinghua.edu.cn (F. Jin).

https://doi.org/10.1016/j.soildyn.2018.07.018
Received 16 September 2017; Received in revised form 23 May 2018; Accepted 14 July 2018

[7,8]). Compared with these simple 2D simulations, 3D numerical simulations have been successful to predict the observed topographic amplification (e.g., [9–11]). In addition, more evidence recently underscores the necessity of modeling coupled effects between topography and subsurface soils, which gives rise to complex wave propagation patterns due to scattering and diffracting of waves within the low-velocity near-surface layers [12–16]. Therefore, coupled 3D topography-soil amplification analyses should be conducted to realistically assess the topographic amplification.

In this study, large-scale numerical simulations are conducted to investigate the influence of topography and subsurface soils on ground motion amplification, using Hong Kong Island as a testbed. Hong Kong is a densely populated region with many buildings and infrastructures built on hill tops and steep slopes due to paucity of land. Owing to the subtropical climate, the volcanic and granitic rocks are subjected to extensive weathering, varying from Grade I (fresh rock) to Grade VI (residual soils) [17]. Therefore, investigating the extent of soil cover and weathered rock profiles in the study region is important. The latest Chinese Seismic Code [4] prescribes a peak ground acceleration of 0.11 g for the 475-year return period motion on “rock” outcrop. It is noted that the obtained design ground-motion are only applicable for a level ground. To date, scientifically based standard for design ground motions on steep slopes is still not available.

Since 3D coupled soil-topography modeling is time-consuming, the overarching goal of the research is to parameterize the ground-motion amplification using simple proxies, such that these effects can be easily incorporated into seismic hazard assessment and design maps. It is only recently that Rai *et al.* [18,19] proposed simple empirical models to incorporate the topographic effects into ground motion prediction models using simple characterization of topography (relative elevation). Note that the study only quantifies the average effects of topography based on regression analysis of strong motion data without considering physical modeling. Another notable recent development includes Maufroy *et al.* [20], who proposed a frequency-scaled curvature as a proxy for topographic amplification based on 3D numerical simulation. The present study will further develop simple parametric models for 3D topography effects by considering additional factors such as the influence of subsurface soils and material damping. The study will immediately benefit Hong Kong and many other areas’ ongoing efforts in assessing topographic amplification of ground motions and seismic performance of infrastructure on steep terrain.

2. Large-scale 3D spectral element simulation

In this study, the 3D Spectral Element Method (SEM) is used for the simulation of wave propagation and topographic amplification on 3D topography. The SEM is a high-order finite element method that uses a special nodal basis. The SEM method is superior to the commonly used finite-difference method in many ways. The SEM uses a pseudo-spectral method to achieve high accuracy in modeling wave propagation. If a polynomial degree of 4 is used (5 interpolation points in each direction), one SEM element per wavelength has been found to be accurate. For example, if the element size is 20 m and shear wave velocity is 200 m/s, the highest frequency that SEM can simulate will be up to 10 Hz, which is important to capture the high-frequency component of ground response. As a comparison, the finite difference method will be very expensive since a great number of grid points will be needed to achieve the same accuracy. The SEM can be easily implemented in parallel computing because its mass matrix is diagonal [21–23]. Because of these advantages, the SEM has been recently widely used in global and regional scale wave simulation with a simulation domain up to hundreds of kilometers [11,24,25].

Fig. 1(a) illustrated an elevation map of Hong Kong Island. The computational domain is the western part of Hong Kong Island with dimensions of 8 km × 9 km. A Digital Elevation Model (DEM) of 0.5 m × 0.5 m resolution is used to extract elevation data in numerical simulations and topographic geometric parameter calculation, which is fine enough to cover very detailed topographic features. The DEM data were collected by means of airborne LIDAR measurement. The highest point in this region, Victoria Peak, is about 554 m above the sea level. The average water depth in Victoria Harbor is around 12 m. The influence of offshore features is considered to be minor when compared with that of the mountain topography. Therefore, the seabed terrain is not considered in the simulation. The illustration of constructed SEM model is shown in Fig. 1(b). The bottom of the numerical model is 100 m deep under the sea level. For most cases of the simulation, the SEM element is chosen as small as 20 m in size using a polynomial degree of 4. Note that the smallest mesh size is chosen according to the highest frequency of the wave considered in the analysis. The actual resolution of the SEM is much less than that of the Digital Elevation Model (0.5 m).

Ricker wavelet is used as acceleration input in the simulation. An uniform ground excitation is input at the base of the model, so the input motion is vertically propagated plane wave. Note that variation of incidence angle is not considered in the present study, which may affect wave amplification of high frequencies according to a recent parametric study [8]. Fig. 2(a,b) shows an example of Ricker wavelet with predominate frequency of 5 Hz and its frequency content. Lysmer-Kuhlemeyer transmitting boundary [26,27] is implemented to mimic the infinite half space at the bottom, and absorbing boundaries are used on the sides to avoid wave reflection from the boundary. As illustrated in Fig. 2(c), a viscous dashpot with a damping coefficient of ρV_s is attached to the lower boundary of the computational domain, where ρ and V_s are the density and shear wave velocity of the truncated base material. Meanwhile, an equivalent shear stress time history, τ_b, is applied at the bottom of the domain,

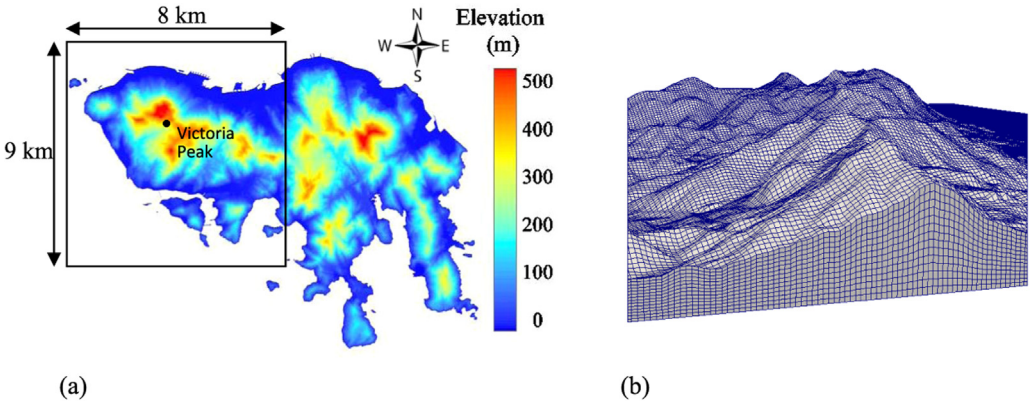

Fig. 1. (a) Hong Kong Island elevation map and study region, (b) Illustration of 3D SEM mesh.

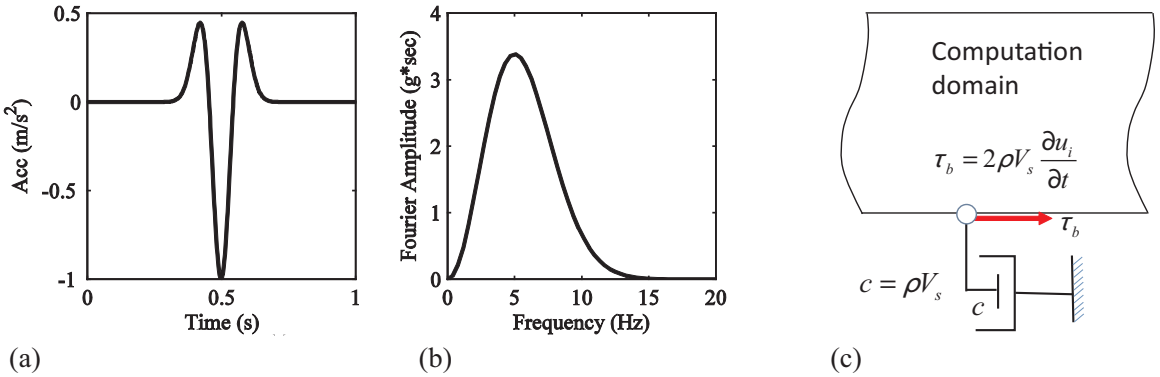

Fig. 2. (a) An example of Ricker wavelet and (b) its frequency content; (c) transmitting boundary.

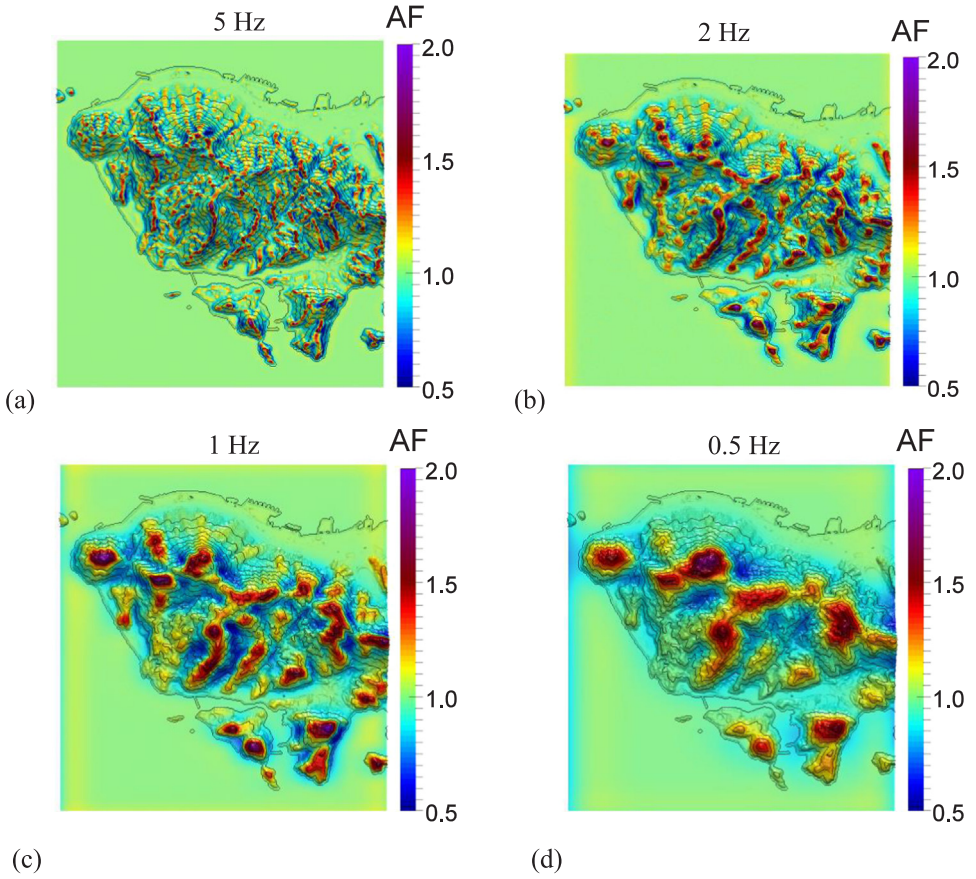

Fig. 3. PGA amplification maps excited by different frequency wavelets. Topography contours are from 0 to 550 m with a 50 m interval.

$$\tau_b = 2\rho V_s \frac{\partial u_i}{\partial t}, \quad (1)$$

where $\partial u_i/\partial t$ is velocity time history of the *incident* wave.

3. Amplification of homogeneous rock case

Recently, Wang *et al.* [25] studied the topographic amplification of ground motions for the western part of Hong Kong Island, by assuming the site is made of homogenous, linearly elastic rock with V_s = 1000 m/s. The ground-motion amplification factor, AF^{3D}_{Rock}, is defined as the PGA on the rock topography surface divided by the PGA on the rock outcrop, which is assumed as a flat ground at zero-level elevation.

Fig. 3 shows amplification factor maps under wavelet excitations with predominant frequencies of 5 Hz, 2 Hz, 1 Hz and 0.5 Hz, respectively. The maximum amplification factor is around 2 for all cases. It is obvious that the amplification/de-amplification is closely related to very localized topographic features under the high frequency (5 Hz) excitation and global topographic features under low frequency (0.5 Hz) excitation. Note that the wavelengths associated with the 5 Hz, 2 Hz, 1 Hz and 0.5 Hz wave are 100 m, 500 m, 1000 m and 2000 m, respectively. The results are in line with the generally accepted notion that long wavelengths mainly influence large features while short ones influence small features. Results also show that amplification generally occurs where convex features are presented and deamplification occurs where concave features are presented. The ground motion amplification factors can be correlated with the following geometric parameters.

3.1. Smoothed topographic curvature

We use the method adopted by Maufroy *et al.* [20] to quantify the

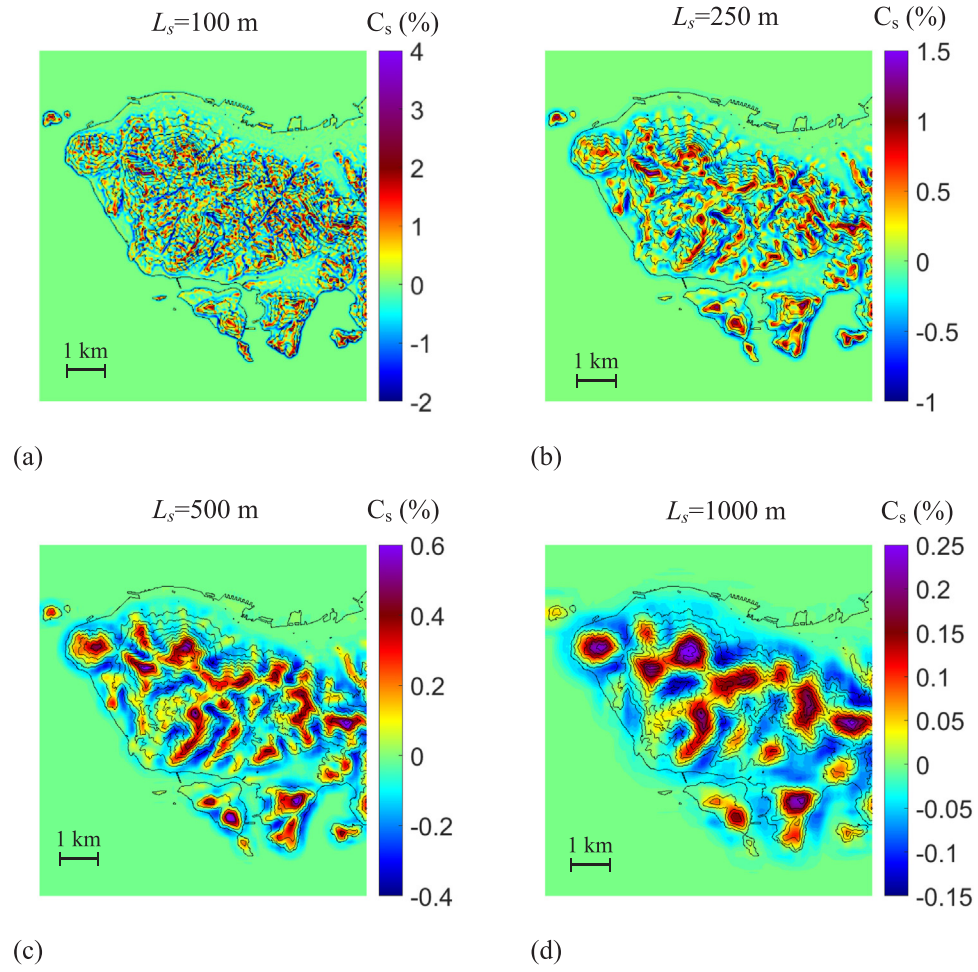

Fig. 4. Smoothed curvature maps using different smoothing lengths. Topography contours are from 0 to 550 m with a 50 m interval.

topographic curvature. In this method, general curvature is defined as the summation of second derivative of elevation in two horizontal directions. If the Digital Elevation Model (DEM) of the region **E** is a rectangular matrix with evenly spaced elevation values with space increment h, the curvature at any point (x_i, y_i) can be computed using the following Eq. (2),

$$\mathbf{C}(x_i, y_i) = \mathbf{E}''(x_i, y_i) \approx -2 \times (\delta + \eta) \times 100, \tag{2}$$

where δ and η are second-order derivative of elevation in x and y directions, which can be approximated by finite difference as

$$\delta = \frac{1}{h^2}\left[\frac{\mathbf{E}(x_{i-1}, y_i) + \mathbf{E}(x_{i+1}, y_i)}{2} - \mathbf{E}(x_i, y_i)\right] \tag{3}$$

and

$$\eta = \frac{1}{h^2}\left[\frac{\mathbf{E}(x_i, y_{i-1}) + \mathbf{E}(x_i, y_{i+1})}{2} - \mathbf{E}(x_i, y_i)\right]. \tag{4}$$

Note that **E** and h should have the same unit (in meters), and the curvature is a point-wise quantity. To account for the influence of length scale, Maufroy *et al.* [20] introduced a smoothed curvature, $\mathbf{C}_s$, by using a box blur smoothing operator, which consists of a double convolution (one per derivative) of matrix **C** with an $n \times n$ matrix of ones:

$$\mathbf{C}_s = \frac{1}{n^4}\left[\mathbf{C}^*\begin{pmatrix}1 & \cdots & 1\\ \vdots & \ddots & \vdots\\ 1 & \cdots & 1\end{pmatrix}_{n\times n}{}^*\begin{pmatrix}1 & \cdots & 1\\ \vdots & \ddots & \vdots\\ 1 & \cdots & 1\end{pmatrix}_{n\times n}\right] \tag{5}$$

when n is dimension of the matrix, $n \times h$ defines the spatial extend of the smoothing operation. The smoothing operation applies two times successively to every entry of matrix **C**. For example, if $n = 3$ and an entry of matrix with an initial value of 50, see Eq. (6), the first smoothing operation averages 3×3 values surrounding that entry and assigned the averaged value to that entry, i.e.

$$\frac{1}{3^2}\begin{bmatrix}40 & 42 & 46\\ 46 & \boxed{50} & 55\\ 52 & 56 & 58\end{bmatrix} * \begin{pmatrix}1 & 1 & 1\\ 1 & 1 & 1\\ 1 & 1 & 1\end{pmatrix} = \begin{bmatrix} & \frac{445}{9} & \end{bmatrix} \tag{6}$$

According to Maufroy *et al.* [20], the smoothing length is defined as $L_s = 2 \times n \times h$, because double convolution has a support size twice as large as the smoothing function. The general curvature maps smoothed over different smoothing lengths are shown in Fig. 4. Apparently, more localized topography (convex/concave) details can be captured if a shorter smoothing length is used.

3.2. Relation between smoothed curvature and topographic amplification factors

Similar patterns in Figs. 3 and 4 suggest a parametric relationship between the ground-motion amplification on homogenous rock and smoothed curvatures. Regression analysis is performed to determine the coefficient of determination R^2 between these two quantities by varying the smoothing length, as shown in Fig. 5. It is found that the amplification factor (AF^{3D}_{Homo}) can be best correlated with the smoothed curvature (C_s), if the smoothing length L_s is half of the input wavelength, i.e., $L_s = \lambda_{Rock}/2$, which is referred to as the "characteristic smoothing

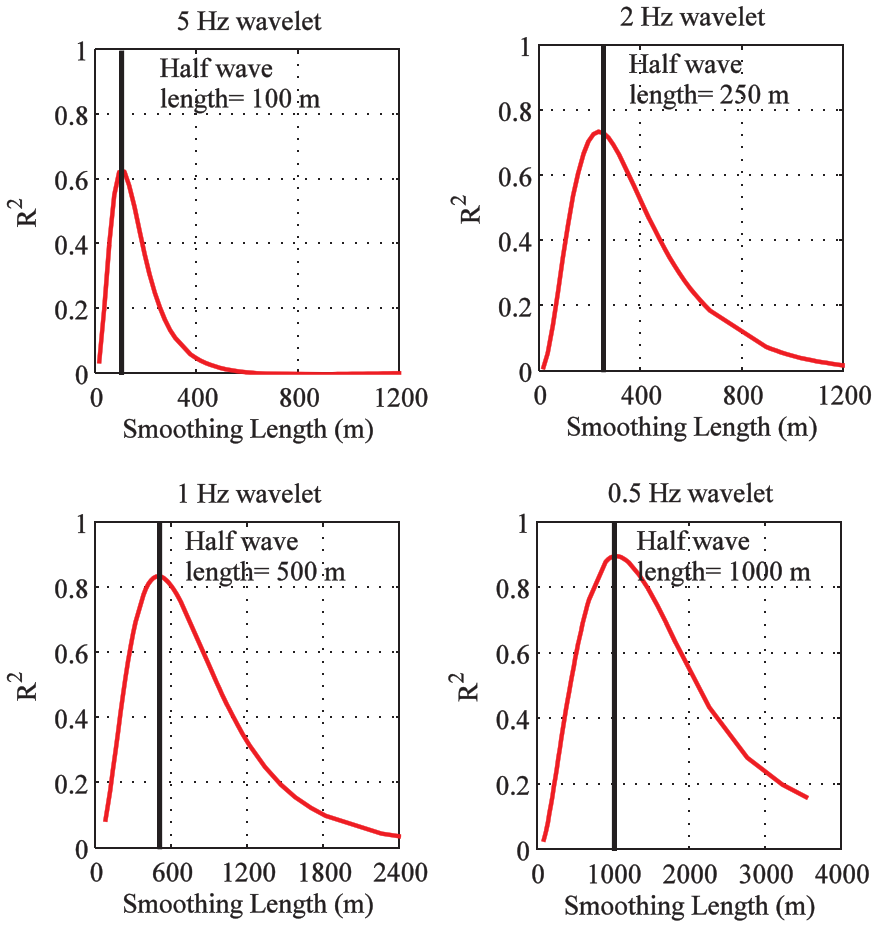

Fig. 5. Coefficient of determination obtained between smoothed curvature over different smoothing lengths and amplification factors.

length".

Fig. 6 shows the correlation between topographic amplification and curvature smoothed over the characteristic length for different frequency excitations. The data can be cast into an exponential form:

$$AF^{3D}_{Rock}(\lambda_{Rock}, C_s) = \exp[a(\lambda_{Rock}) \times C_s(L_s)] \quad (7)$$

where $a(\lambda_{Rock}) = 9.24 \times 10^{-4}\lambda_{Rock}$, and C_s (L_s) is the curvature smoothed over the characteristic length $L_s = \lambda_{Rock}/2$. The term λ_{Rock} is the wavelength in rock (unit in meter), which can be determined by shear wave velocity in rock ($V_{s,Rock}$) and excitation frequency (f) via $\lambda_{Rock} = V_{s,Rock}/f$. Eq. (7) manifests that the frequency-dependent amplification is related to a scale-dependent topographic feature, similar to the findings reported by Maufroy *et al.* [20]. Amplification of high frequency wave is correlated with curvature smoothed over a small length scale. On the other hand, amplification of long-period waves is correlated with large-scale topography features. It is worth pointing out that for higher frequency wave, R^2 of the correlation becomes smaller, i.e., Eq. (7) is more accurate for long-period waves. As shown in Fig. 6(d), all the fitting curves pass through the point of (0,1), which is reasonable because for the special case when the surface is flat ($C_s = 0$), there is no amplification or deamplification.

3.3. Topographic relative elevation

Apart from smoothed curvature, relative elevation (H_r) is another commonly used parameter for land surface geometry [18,19]. H_r is defined as the difference between the elevation at a point and the mean value of the evaluations within a specified neighborhood. In this study, we use a square neighborhood with the length defined as L_h. The parameter is effective to represent topographic features. A positive H_r value indicates features such as ridges and a negative H_r is for valleys. The relative elevation maps calculated over different length scales are shown in Fig. 7.

Regression analysis is performed to determine the correlation between the smoothed curvature and the relative elevation. As shown in Fig. 8(a), the R^2 between C_s and H_r is calculated for different L_s and L_h respectively. It is found that the best correlation is obtained when $L_h = 1.5 \times L_s$ and the corresponding R^2 is as high as 0.94. Fig. 8(b) shows an example of the strong correlation between C_s and H_r with $L_h = 750\ m$ and $L_s = 500\ m$. A linear function can be used to describe this relationship given $L_h = 1.5 \times L_s$,

$$C_s = \left(\frac{1.095 \times 10^3}{L_s^2}\right) \times H_r \quad (8)$$

Therefore, it can be concluded that the smoothed curvature and the relative elevation for given length scales represent similar information about the topography. Either of them can be used in developing parametric models, and Eq. (8) can be used to conveniently convert one to the other.

4. Influence of subsurface soils on topographic amplification

Due to extensive weathering of in-situ rock, residual soils often exist at the topographic surface. The influence of subsurface soils on ground-motion amplification is considered in the following study. At the present stage, the soil is assumed to be linearly elastic without considering nonlinearity, and the depth of the soil layer is uniform overlying the rock. The shear wave velocity is assumed to be 200 m/s, which is a typical value for residual soils in Hong Kong [17]. Thus, the wavelength in soil layer is 1/5 of that in rock, i.e., $\lambda_{Soil} = 1/5\lambda_{Rock}$. The predominant

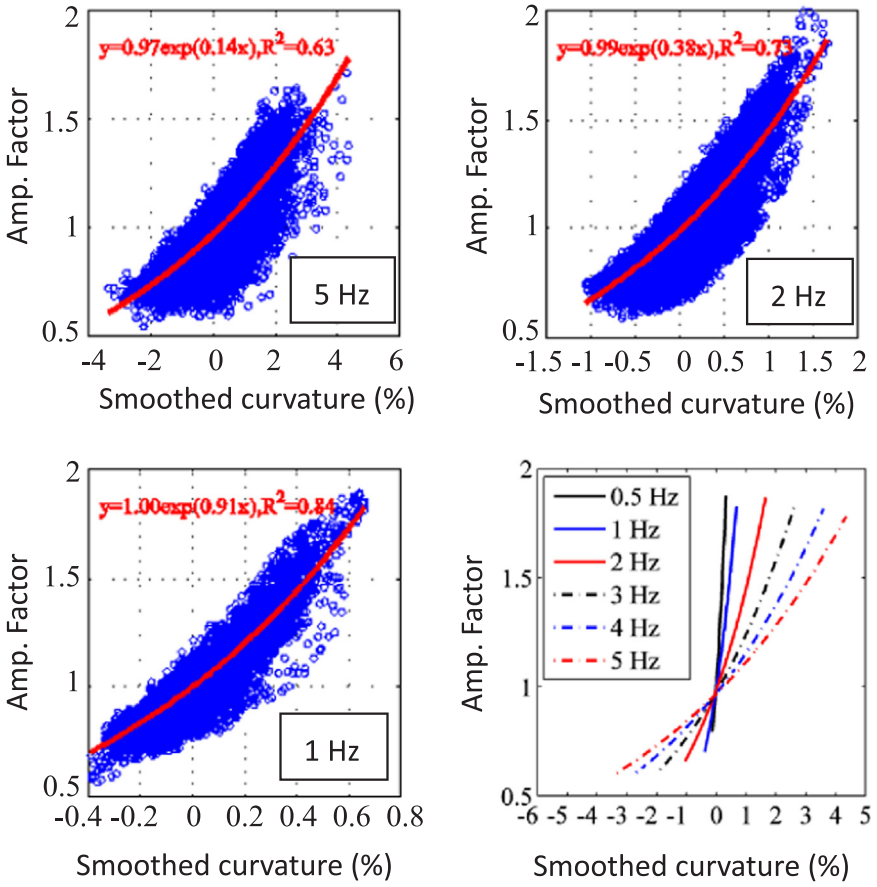

Fig. 6. Correlation between amplification factor and curvature smoothed over characteristic smoothing length ($L_s = \lambda_{Rock}/2$) for different frequency excitations.

frequencies of the input wavelet are 5 Hz, 2 Hz, 1 Hz and 0.5 Hz, respectively. Accordingly, the corresponding wavelength in soil λ_{Soil} equals to 40 m, 100 m, 200 m and 400 m, respectively. For the soil case under 5 Hz excitation, we used a finer horizontal mesh of 10 m and smaller domain to compensate for the simulation time.

4.1. Amplification on layered soils

The topographic amplification factor, *TAF*, is defined using the following Eq. (9),

$$TAF = AF^{3D}_{Layered}/AF^{1D}_{Layered}, \quad (9)$$

where $AF^{3D}_{Layered}$ is the PGA on 3D topography surface of layered soils against the PGA on rock outcropped at zero-level elevation, $AF^{1D}_{Layered}$ is the PGA on horizontally layered soil against the PGA on the rock outcrop. $AF^{1D}_{Layered}$ shows the amplification of the soil layer without considering the topographic effects, and it can be easily obtained by 1D site response analyses. By normalizing the 1D soil amplification, *TAF* reflects topographic amplification factor coupled with subsurface soils.

Fig. 9 shows the soil amplification obtained from 1D response analyses. As expected, the amplification factors coincide for different input frequencies if the soil depth is normalized by the wavelength λ_{Soil}. The $AF^{1D}_{Layered}$ yields a peak value of 2.35 when the soil depth equals to $0.2\lambda_{Soil}$. The peak value corresponds to the natural frequency of the soil layer, which would occur at the soil depth equal to $0.25\lambda_{Soil}$.

The *TAF* factors under 1 Hz excitation are shown in Fig. 10. Four cases with different soil depths are illustrated, including the homogeneous rock case ($SD = 0$ m) and cases with the soil depths of 20 m, 40 m and 60 m, respectively. Due to existence of surface soils, the amplification pattern has changed significantly compared with the homogeneous rock case, which is closely correlated to large-scale topographic features. With an increasing soil depth, the amplification zones become narrower, although they are still around the mountain ridges, as shown in Fig. 10 (a) and (b). If the soil depth further increases, the amplification pattern generally changes to the case of a homogeneous soil site, with the amplification pattern more closely correlated to small-scale topographic features, i.e., curvatures smoothed using a smaller smoothing length. This is reasonable because the wavelength in the surface soils is 1/5 of that in rock, $\lambda_{Soil} = 1/5\lambda_{Rock}$, therefore, the presence of the soil layer tends to be influenced by small-scale topographic features. It is also interesting to notice that when the soil depth is greater than a certain threshold, the amplification pattern will no longer change significantly and can be approximated as a homogeneous soil case.

4.2. Influence of subsurface soil depth on characteristic smoothing length

In order to obtain the characteristic smoothing length for the layered case, parametric study has been conducted using 5 Hz, 2 Hz, 1 Hz and 0.5 Hz wavelet excitation by assuming different soil depths. The results are compared with the homogenous rock case ($SD = 0$ m) as shown in Fig. 11, where the characteristic smoothing length for homogenous rock case ($L_s = 1/2\lambda_{Rock}$) is highlighted using a solid line for each case.

It is observed that the characteristic smoothing length (corresponding to the maximum R^2) becomes smaller with an increasing soil depth. This is due to the fact that λ_{Soil} is much shorter than λ_{Rock}, therefore, the size of influenced features should be smaller. Moreover, the maximum R^2 also decreases with an increasing soil depth. When the soil reaches a certain depth, no significant change is observed for the characteristic smoothing length and its associated R^2.

Finally, the relation between the modified characteristic smoothing

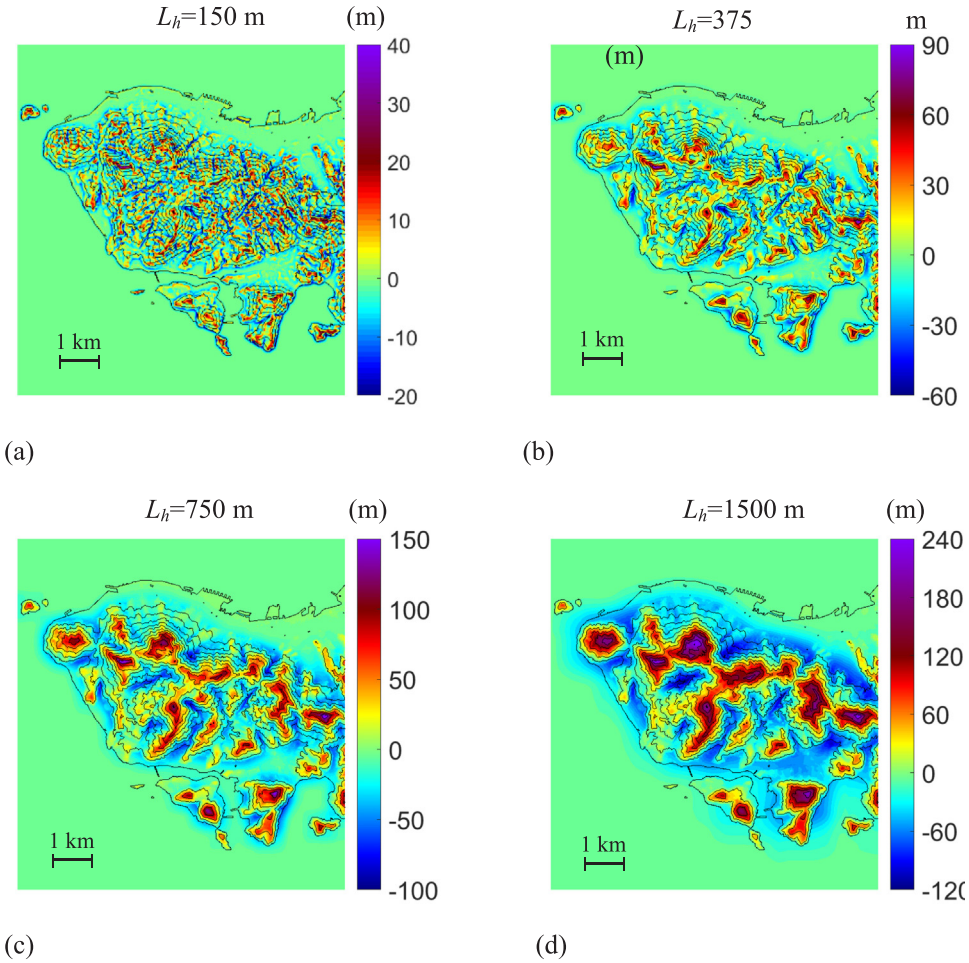

Fig. 7. Relative elevation maps calculated over different scale lengths. Topography contours are from 0 to 550 m with a 50 m interval.

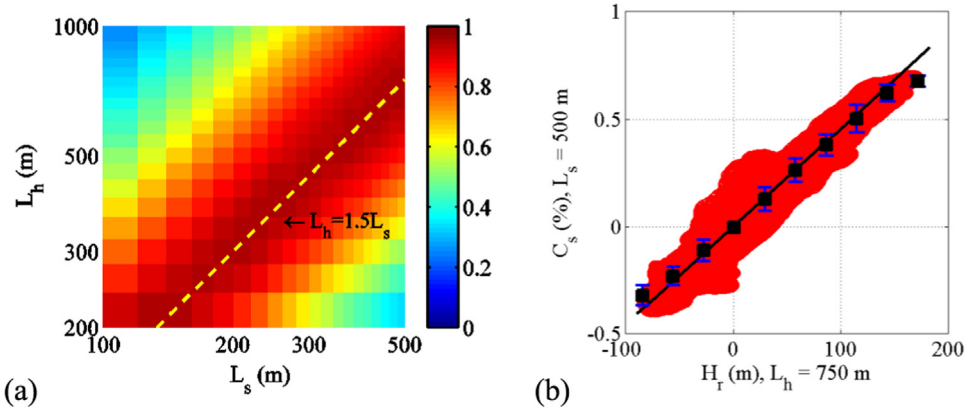

Fig. 8. (a) Coefficient of determination obtained between the smoothed curvature and the relative elevation for different L_s and L_h; (b) An example showing C_s vs H_r for L_s = 500 m and L_r = 750 m. A linear fitting line and error bars (mean ± 1 std) are also plotted.

length (L_s) and soil depth (SD) is shown in Fig. 12. If L_s and SD are normalized by λ_{Soil}, a rather consistent relationship can be obtained for different wave frequencies. For the layered site, L_s decreases linearly from 2.5 λ_{Soil} (corresponding to a homogenous case 0.5 λ_{Rock}) to 0.5 λ_{Soil}(corresponding to a homogenous soil case), when the soil depth increases from 0 to 0.2 λ_{Soil}. Beyond that depth limit, L_s remains to be unchanged. A simplified fitting curve, shown as the dash red line in Fig. 12(b), can be used to describe the unified relationship for different input wave frequencies.

It is important to note that 0.2 λ_{Soil} correspond somewhat to the natural frequency of the soil column, which would occur at SD= 0.25 λ_{Soil} for the first mode. This implies the relationship between the soil depth and the shear-wave velocity of the subsurface soils is very important in quantifying the effect of topographic amplification.

4.3. Prediction equation for topographic amplification

Although it is tempting to use a simple functional form, such as Eq.

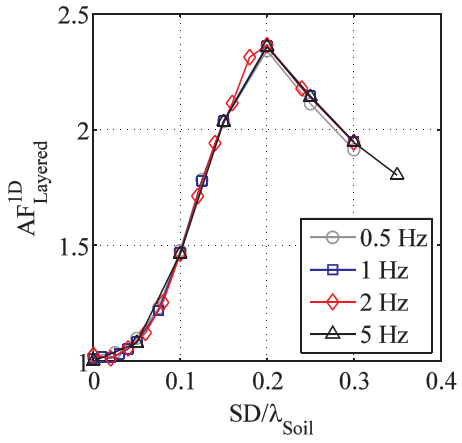

Fig. 9. $AF^{1D}_{Layered}$ computed using 1D site response analyses.

(7), to predict the amplification factor for the layered soil case, the model exhibits considerable bias in its residuals against slope angles. As shown in Fig. 13(a)(b), the residual is not biased over curvature, yet, they has a clear trend against the slope angles, especially when the slope angle is greater than 15°. The spatial distribution of the residuals show a similar pattern as the map of the slope angle, as shown in Fig. 13(c)(d).

Therefore, the *TAF* prediction can be significantly improved by introducing a linear term with respect to slope angles as follows:

$$\ln(TAF)_{undamped} = \ln\left(\frac{AF^{3D}_{Layered}}{AF^{1D}_{Layered}}\right) = \begin{cases} a(SD)\times C_s(L_s)+\varepsilon, & for\ \theta < 15^\circ \\ a(SD)\times C_s(L_s)+b(SD)\times(\theta-15^\circ)+\varepsilon, & for\ \theta \geq 15^\circ \end{cases} \quad (10)$$

where SD is the soil depth (in m), $a(SD)$ and $b(SD)$ are parameters dependent on SD, $C_s(L_s)$ is the curvature smoothed over the characteristic length shown in Fig. 12, θ is the slope angle (in degree), and ε is the residual that follows a normal distribution with a zero mean and a standard deviation of $\sigma = \text{std}(\varepsilon)$□

The $a(SD)$ and $b(SD)$ values for different wavelet frequencies and soil depths have been computed through regression analyses as illustrated in Fig. 14. If these two parameters are normalized by the wavelength in soil λ_{Soil}, a unified relation can be obtained for these two parameters, as represented by the red dash lines in Fig. 14. The parameter $a(SD)$ for the curvature decreases when the soil depth is less than 0.2 λ_{Soil} and remains as a constant for deeper soils. The parameter $b(SD)$ for the slope angle first decreases and then increases to zero. A minimum value of b (termed as b_0) occurs when the soil depth is 0.15 λ_{Soil}. This trend also indicates that when the soils are deeper than 0.3 λ_{Soil}, the slope angle has minor influence on topographic amplification. The b value assumes zero for that case.

Fig. 14(c) further illustrates dependency of b_0 on the wavelength in soils. It is worth pointing out that the absolute value of b_0 linearly decreases if the wave wavelength increases from 40 m~400 m, i.e, when frequency reduces from 5 Hz to 0.5 Hz. For wave frequencies less than 0.5 Hz, the influence of the slope angle can be neglected.

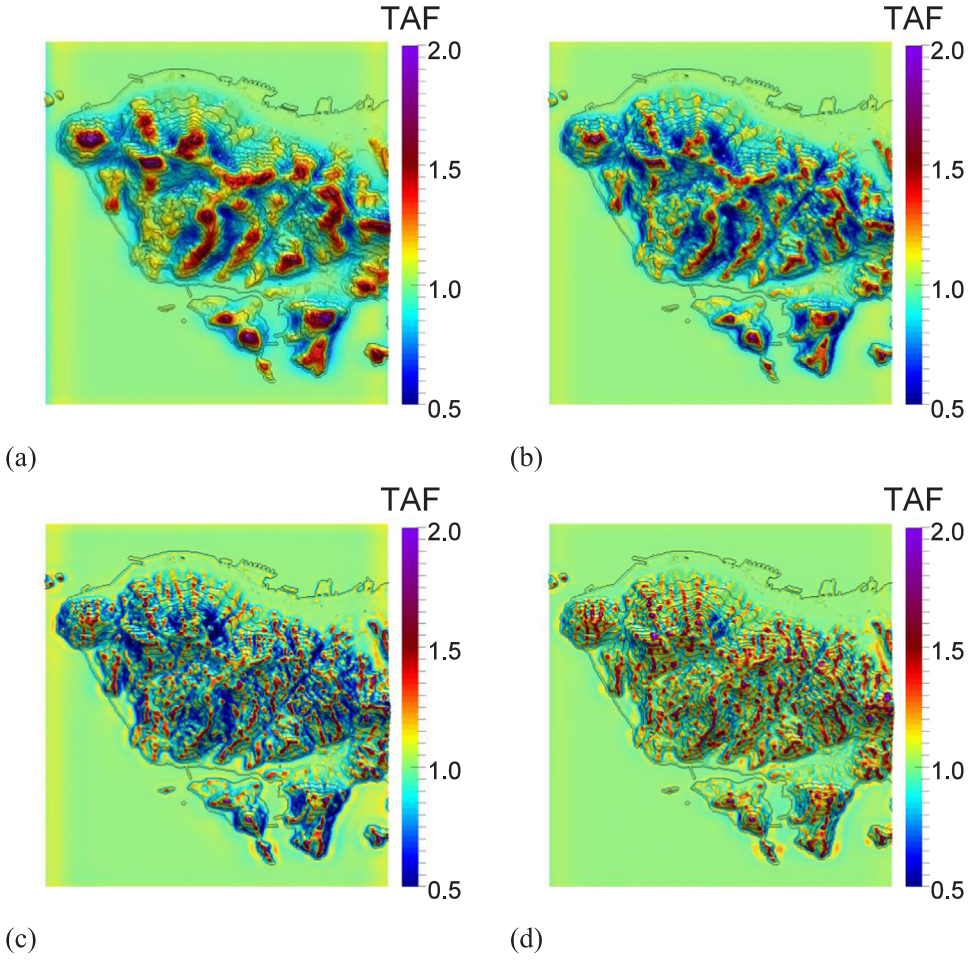

Fig. 10. *TAF* maps of layered soils with different soil depths under 1 Hz wavelet excitation. Topography contours are from 0 to 550 m with a 50 m interval.

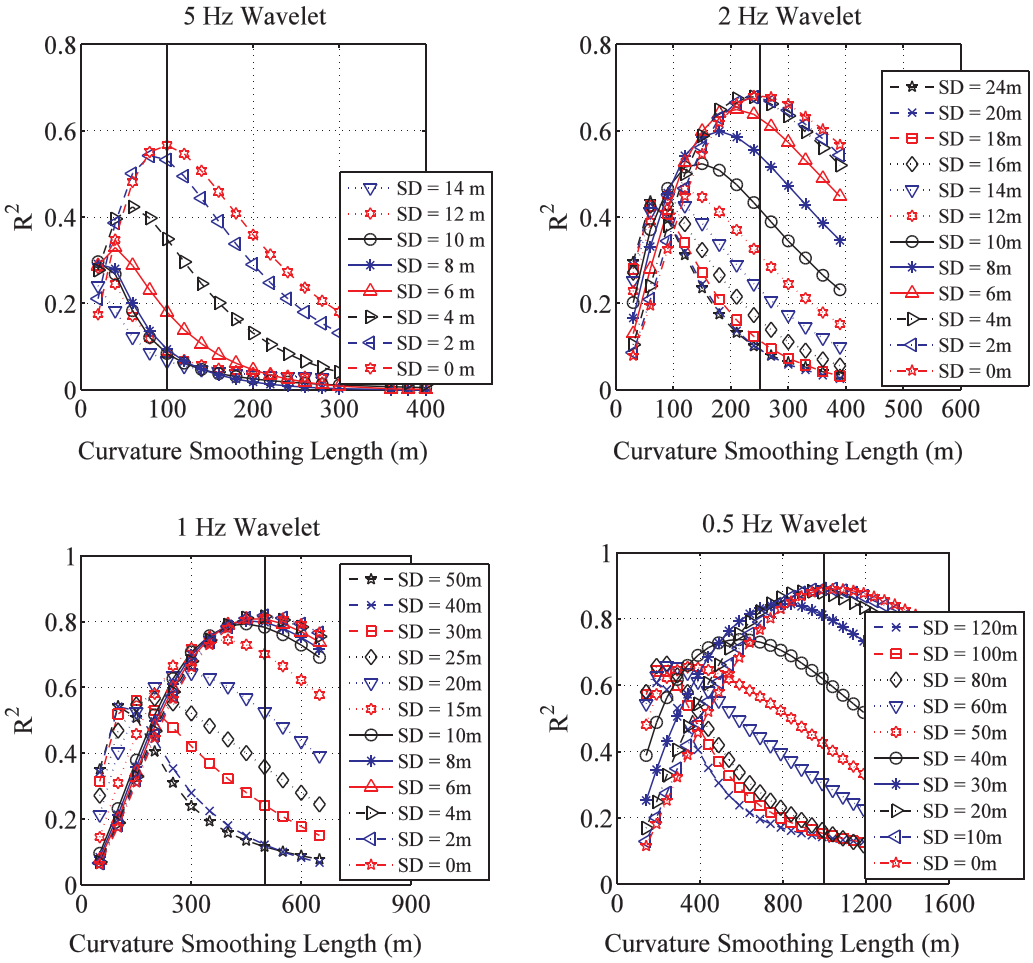

Fig. 11. R^2 obtained between different smoothing lengths and *TAF* factors.

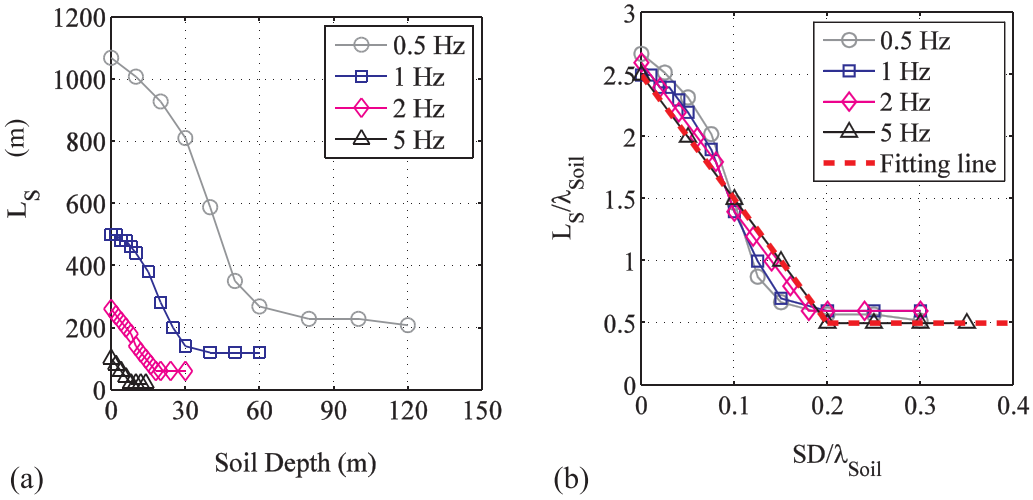

Fig. 12. Modified characteristic length for the layered soil with different soil depths.

Statistical analyses are performed to evaluate the importance of the slope angle in the prediction. As shown in Fig. 15, adding the slope angle term could improve the coefficient of determination R^2 and reduce the standard deviation of residuals considerably. The improvement is most significant when the soil depth is within the range of $(0.1–0.2)\lambda_{Soil}$. In general, the standard deviation of Eq. (10) falls into the range of 0.1–0.15, which slightly increases with the increase of soil depth.

5. Influence of material damping

In the previous section, the soil and rock are assumed to be uniform and linearly elastic without damping, yet damping should be considered for more realistic cases. For a 1D harmonic plane wave, the motion in undamped elastic media can be written as [28]:

$$u = u_0 \exp[i(\omega t - \kappa Z)] \tag{11}$$

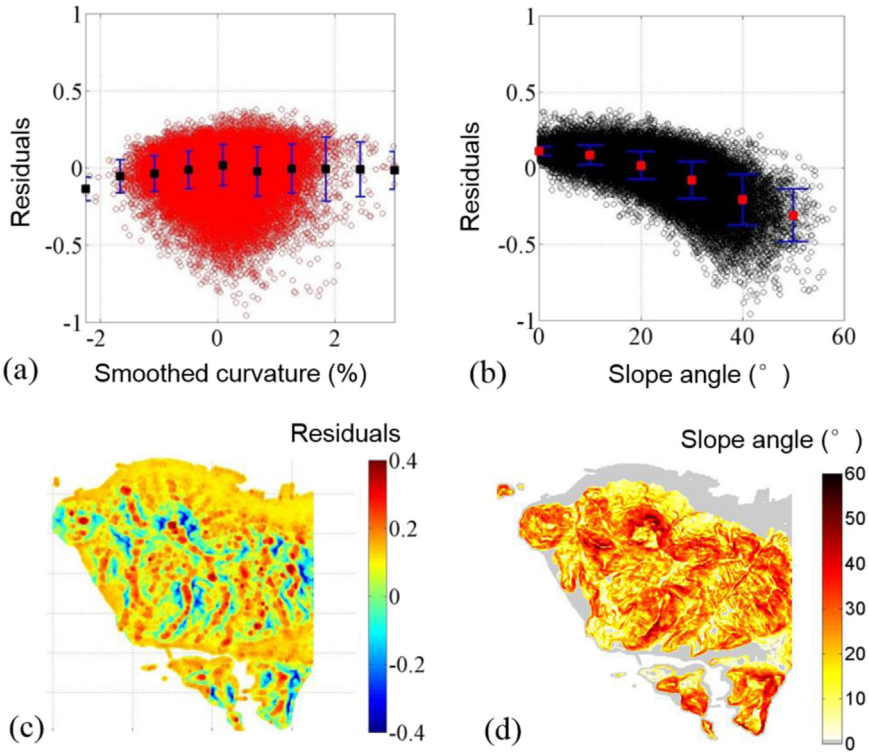

Fig. 13. Residual analysis of *TAF* under 2 Hz wavelet and SD = 10 m: (a) residuals against curvature, (b) residuals against slope angle; (c) spatial distribution of residuals, (d) slope angle map.

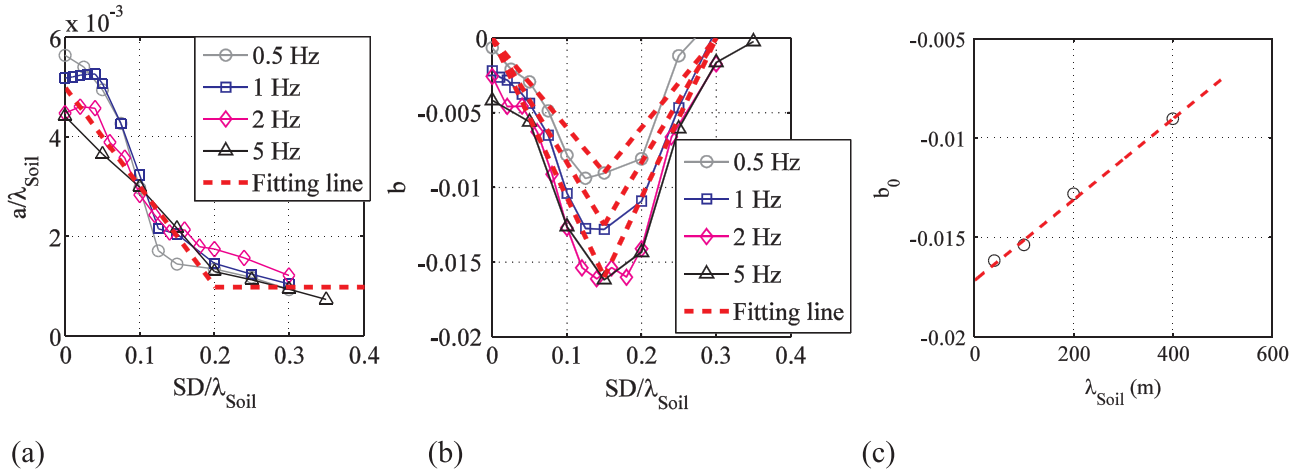

Fig. 14. Parameters (a) $a(SD)$ and (b)$b(SD)$ derived with different soil depths and input wavelet frequencies; (c) Dependence of b_0 on the wavelength in soils.

where u_0 is the displacement amplitude, ω is the angular frequency, κ is the wave number ($\kappa = 2\pi/\lambda$) and Z is wave traveling distance. For the case of vertically propagated wave, Z represents the elevation. If the material damping is considered, the wave solution can be written as

$$u = u_0 exp(-\alpha Z)\exp[i(\omega t - \kappa Z)] \quad (12)$$

where $\alpha = (\sqrt{Q^2 + 1} - Q)\kappa \approx \zeta\kappa$ is the attenuation factor, Q is the quality factor, and ζ is the damping ratio. Theoretical solutions of Eqs. (11) and (12) show that the amplitude of the harmonic wave decays exponentially along traveling path with an amplitude multiplier of $exp(-\alpha Z)$, as illustrated in Fig. 16.

5.1. Amplifications of homogenous rock with damping

Large scale numerical simulations have been also conducted to study the topographic amplification of ground motions with material damping. In the SEM simulation, standard linear solids are used to achieve constant damping over the frequency range of interest [23]. For a homogenous rock site, the rock damping is assumed to be constant, varying from 1% to 3%. Predominant frequencies of the input wavelets are 5 Hz, 2 Hz, 1 Hz and 0.5 Hz, respectively. The amplification factors are shown in Fig. 17 for illustration purpose.

It can be observed that the amplitude decays with an increasing elevation for different damping ratios. According to the theoretical solution, the wave function in viscoelastic material can be treated as the wave function in an undamped elastic medium multiplied by an attenuation factor, $exp(-\alpha Z)$. Dividing the amplification factor from the viscoelastic simulation by that from undamped elastic simulation, we can derive the attenuation factor from the numerical simulations, which is compared with that from theoretical solution in Fig. 18. Results show that although topographic features are present in the 3D model, the

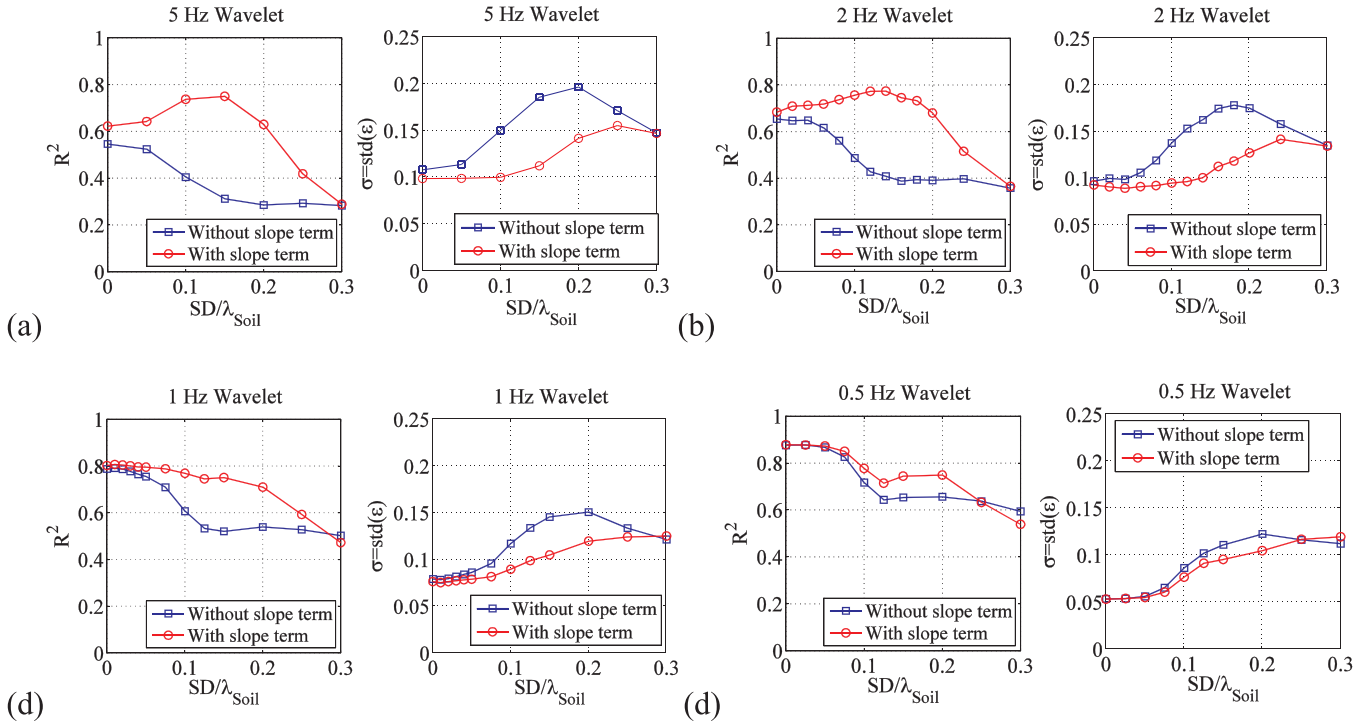

Fig. 15. R^2 and standard deviation of residual obtained using prediction equation with and without the slope term.

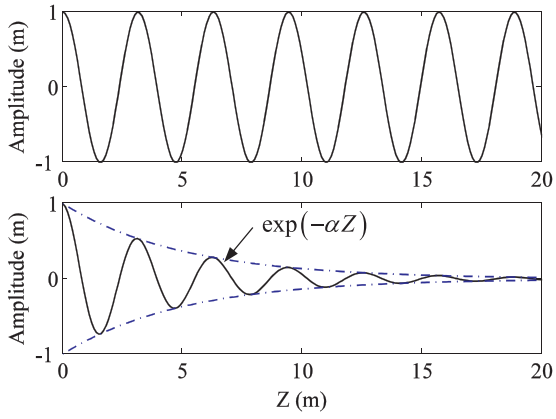

Fig. 16. Theoretical attenuation of harmonic plane wave in elastic and viscoelastic materials.

derived attenuation factor α generally follows theoretical solution. The good match of Fig. 18 is probably because a single pulse is used in the simulation, and multiple scattering due to various input cycles is neglected. Another reason may due to the fact that the wave mainly propagates vertically. Therefore, the elevation Z becomes a good indictor to measure the wave travel distance and associated damping effects. For these special cases, the damping effects can be decoupled from the topographic effects, and theoretical attenuation factor can be used for approximation of ground motion amplifications.

Therefore, if the material damping is considered, the prediction equation Eq. (7) can be modified by adding a damping term as follows

$$AF^{3D}_{Rock}(\lambda_{Rock}, C_s) = \exp[a(\lambda_{Rock}) \times C_s(L_s)] \times \exp\left(-\frac{2\pi}{\lambda_{rock}}\zeta Z\right) \quad (13)$$

where ζ is the damping ratio and Z is the terrain elevation (in m, assume the elevation of rock outcrop is 0 m). The standard deviations of the model residuals, $\sigma = \text{std}(\varepsilon)$, are generally less than 0.1.

5.2. Influence of material damping on layered soils

A more realistic scenario is now considered for a viscoelastic soil layer with a uniform depth overlying a viscoelastic rock site. The properties of the soil is same as that in Section 4, i.e. shear wave velocity is assumed to be 200 m/s. Therefore, $\lambda_{Soil} = 1/5\lambda_{Rock}$. The damping ratio of the soil, ζ_{Soil}, is assumed as 10% and the damping ratio of the rock, ζ_{Rock}, is 1%. Recall Eq. (9), the topographic amplification factor, *TAF*, is defined as the amplification on 3D layered topography divided by the 1D amplification factor with material damping considered in both cases, i.e., $(TAF)_{damped} = (AF^{3D}_{Layered}/AF^{1D}_{Layered})_{damped}$. The normalization eliminates the effect of 1D soil amplification and soil damping. Finally, the topographic amplification factor for the damped case can be related to the undamped case through the following relationship:

$$(TAF)_{damped} = (TAF)_{undamped} \exp\left(-2\pi\zeta_{rock}\frac{Z}{\lambda_{rock}}\right) \quad (14)$$

where only rock damping, ζ_{rock}, is involved and Z is the elevation ($Z = 0$ for the rock outcrop). The amplification maps under 1 Hz wavelet excitation are shown in Fig. 19.

Finally, the general prediction equation can be established as:

$$ln\left(\frac{AF^{3D}_{Layered}}{AF^{1D}_{Soil}}\right)_{damped} = \begin{cases} a(SD) \times C_s(L_s) - 2\pi\zeta_{rock}\left(\frac{Z}{\lambda_{rock}}\right) + \varepsilon, & for\ \theta < 15 \\ a(SD) \times C_s(L_s) + b(SD) \times (\theta - 15) - 2\pi\zeta_{rock}\left(\frac{Z}{\lambda_{rock}}\right) + \varepsilon, & for\ \theta \geq 15 \end{cases} \quad (15)$$

where L_s, $a(SD)$ and $b(SD)$ depend on the soil depth and wavelength, as shown in Figs. 12 and 14. θ is slope angle (in degree), Z is elevation and ζ_{rock} is rock damping. The derived R^2 and standard deviation of residuals σ for Eq. (14) is shown in Fig. 20, which are similar as the results in Section 4.3 (Fig. 15). The parametric model gives quite accurate results with a standard deviation of residuals generally falling in the range of 0.1–0.15. It is worth pointing out that Eq. (15) essentially represents topographic amplification that is frequency dependent, as the wavelength is simply related to wave frequency via $\lambda = V_s/f$.

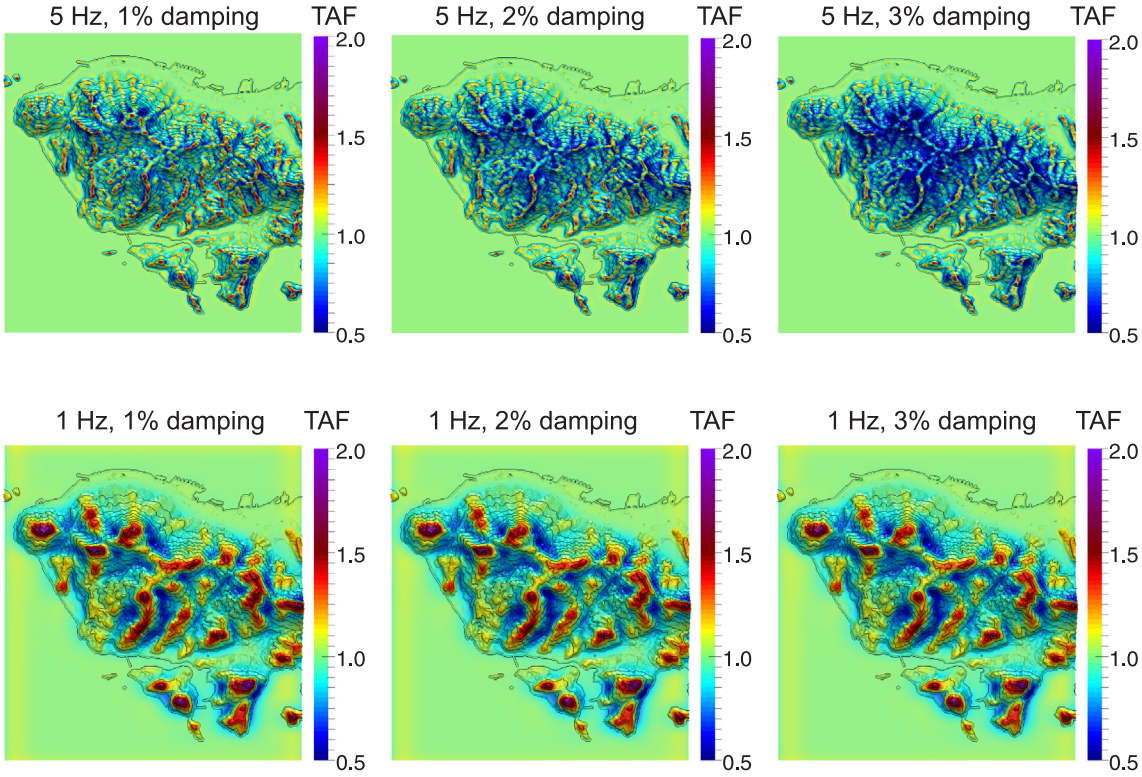

Fig. 17. *TAF* maps for homogenous rock cases with different damping ratios, excited by 5 Hz and 1 Hz wavelet.

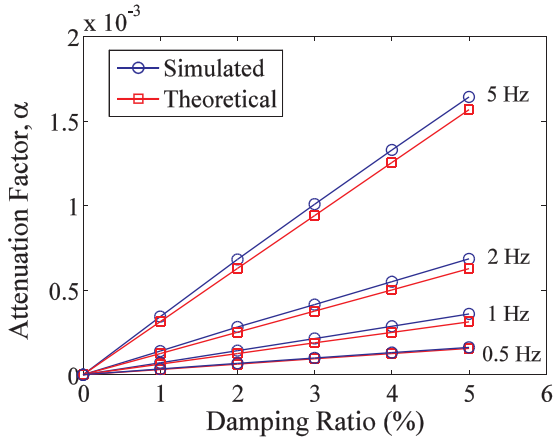

Fig. 18. Attenuation factor α obtained from theoretical solution and simulation results.

6. Conclusions and discussions

In this study, a region-scale 3D numerical simulation has been conducted to quantify ground-motion amplification considering 3D topography and subsurface soils, using Hong Kong Island as a testbed. The numerical analyses revealed that the topographic amplification is frequency dependent. If the site is made of homogenous rock, the topographic amplification is best correlated with topographic curvature smoothed over a characteristic length, which equals to half of the wavelength in rock. Amplification of the high-frequency wave is correlated with curvature smoothed over a small length scale, and amplification of long-period waves is correlated with large-scale topography features in horizontal dimension. The maximum topography amplification generally ranges from 1.6 to 2.0 in the protruded areas. Deamplification of the high-frequency wave is observed in the locally concaved areas even at high elevations. Results obtained from the 3D analysis are generally greater than those obtained from 2D analyses.

Considering a layer of low-velocity subsurface soil, the topographic amplification factor (*TAF*) is significantly influenced by thickness of the soil layer and wavelength, even though *TAF* is normalized by 1D soil amplification. Compared with the homogeneous rock case, the amplification pattern becomes more closely correlated to small-scale features as the layer thickness increases, which is due to the fact that the wavelength in soil is relatively short. When both topography amplification and soil amplification are considered, the total amplification factor (compared with the rock outcrop) could be greater than 4 if the soil depth is around $0.2\lambda_{Soil}$. The study also demonstrates that the effect of material damping can be decoupled from the topographic amplification, and can be modeled using a theoretical attenuation factor for 1D plane wave propagation parameterized by terrain elevation. Based on numerical simulation, parametric models were proposed to quantify the topographic amplification considering subsurface soils, material damping and input wave frequencies. The model is parameterized by the curvature smoothed over a modified characteristic length, the slope angle and the terrain elevation, and provides accurate predictions on the topographic amplification with a standard deviation of residuals in the range of 0.1–0.15.

Admittedly, wave interference over topography is a complicated nonlinear process. A more comprehensive picture of the surface and subsurface topography is needed to consider all wave interference. It should be noted that the smoothed curvature, which demonstrated certain efficiency in predicting amplification for homogenous rock cases, becomes less effective to capture the physics behind when soil layers are considered. This is clearly shown by low R^2 values especially for higher frequencies and larger soil depths (Fig. 11).

For simplicity, wavelet pulses are used as input motions in this study, whose durations are much shorter than real earthquake motions. The simplification may lead to underestimation of the topographic amplification. In addition, the soil stratum is assumed with a constant thickness and stiffness. The sharp contrast existed between the soft soil layer and the rock base may exacerbate the soil resonance effects.

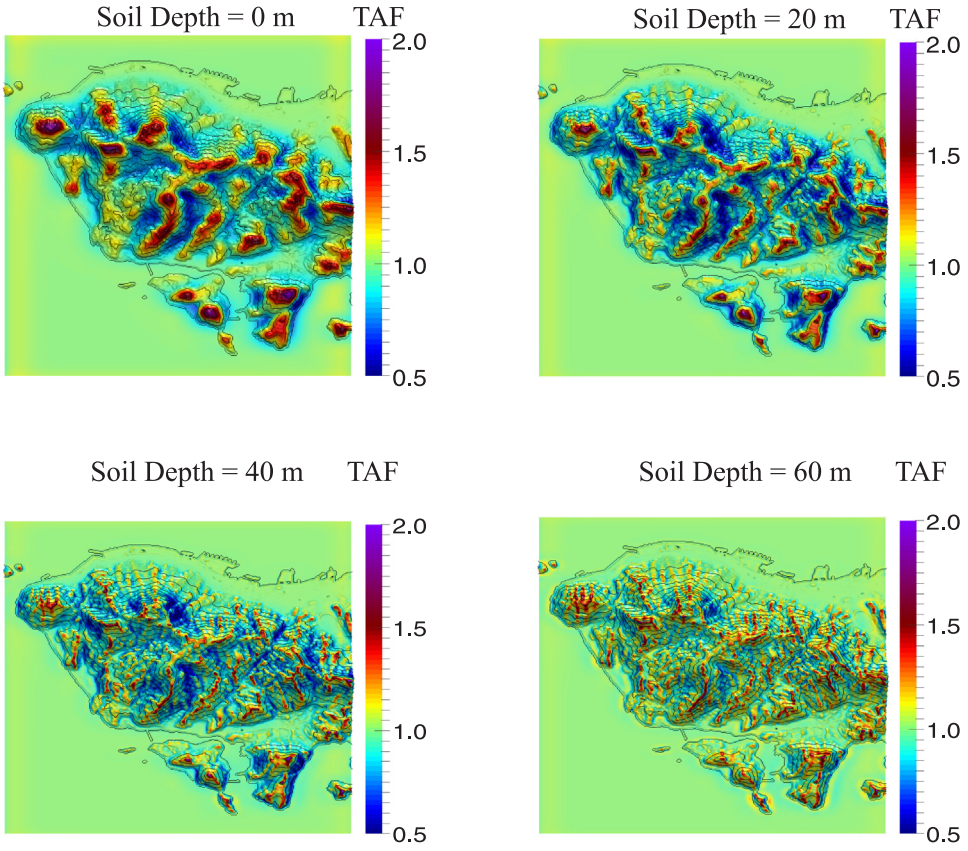

Fig. 19. *TAF* maps on layered soils with different soil depths under 1 Hz wavelet. The damping ratio of soil ζ_{Soil} is 10% and the damping ratio of rock ζ_{Rock} is 1%. Topography contours are from 0 to 550 m with a 50 m interval.

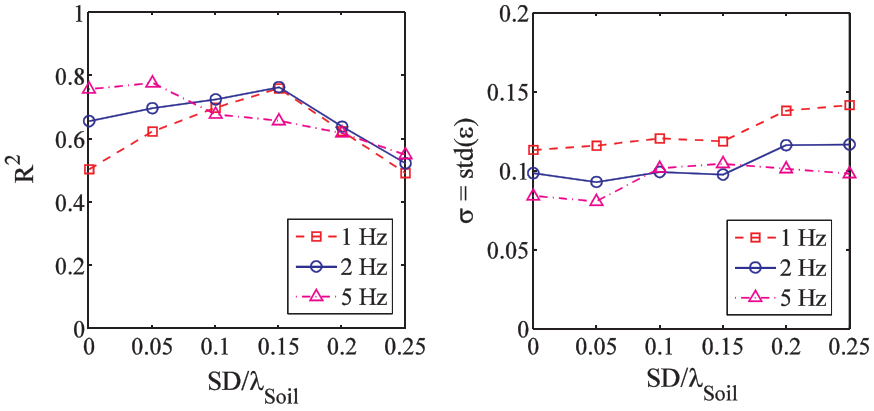

Fig. 20. R^2 and standard deviation of residual obtained using the general prediction equation.

Realistic layering with gradually changed soil profile may result in different scattered wavefield and amplification pattern. At the present, we are collecting and reviewing thousands of borehole information in order to model realistic near-surface geology of the study area. Emphasis will be placed on investigating the variation of soil cover and weathered rock profiles on the hill top and hill slope, which may have great impact on site amplification as revealed by this study.

Further, the spatial correlation of soil properties needs to be investigated using geostatistics analyses, such as the co-kriging technique [29,30], in order to interpolate data at locations without direct measurement. Extensive parametric study needs to be performed to quantify the uncertainty and variability of the ground-motion amplification through varying stratification and properties of soil/rock units. Recorded or simulated ground motions (such as [31,32]) need to be used to examine the effects of ground motion duration, energy/frequency content and nonstationary on topographic amplification. The proposed topographic amplification models can be combined with Newmark displacement analysis [33–35] to assess regional co-seismic landslide hazards. These topics will be addressed in future studies.

Acknowledgements

The study was supported by the Hong Kong Research Grants Council (RGC) through the General Research Fund grant no 16214118, 16213615 and National Natural Science Foundation of China grant no. 51639006. This paper is published with the permission of the Head of the Geotechnical Engineering Office and the Director of Civil Engineering and Development, the Hong Kong SAR Government.

References

[1] Lee VW. Three-dimensional diffraction of plane P, SV and SH waves by a hemispherical alluvial valley. Soil Dyn Earthq Eng 1984;3(3):133–44.
[2] Spudich P, Hellweg M, Lee WH. Directional topographic site response at Tarzana observed in aftershocks of the 1994 Northridge, California, earthquake: implications for mainshock motions. Bull Seismol Soc Am 1996;86(1B):S193–208.
[3] Trifunac MD, Hudson DE. Analysis of the Pacoima dam accelerogram—San Fernando, California, earthquake of 1971. Bull Seismol Soc Am 1971;61(5):1393–411.
[4] Ministry of Construction of P.R. China. Code for seismic design of buildings. Beijing, China: China Architecture & Building Press; 2010. [in Chinese].
[5] CEN. Eurocode 8: Design provisions for earthquake resistance of structures. Part 5: Foundations, retaining structures and geotechnical aspects, Brussels, Belgium; 1998.
[6] Burjánek J, Edwards B, Fäh D. Empirical evidence of local seismic effects at sites with pronounced topography: a systematic approach. Geophys J Int 2014;197(1):608–19.
[7] Ashford SA, Sitar N, Lysmer J, Deng N. Topographic effects on the seismic response of steep slopes. Bull Seismol Soc Am 1997;87(3):701–9.
[8] Poursartip B, Fathi A, Kallivokas LF. Seismic wave amplification by topographic features: a parametric study. Soil Dyn Earthq Eng 2017;92:503–27.
[9] Paolucci R, Faccioli E, Maggio F. 3D response analysis of an instrumented hill at Matsuzaki, Japan, by a spectral method. J Seismol 1999;3(2):191–209.
[10] Smerzini C, Paolucci R, Stupazzini M. Comparison of 3D, 2D and 1D numerical approaches to predict long period earthquake ground motion in the Gubbio plain, Central Italy. Bull Earthq Eng 2011;9(6):2007–29.
[11] He CH, Wang JT, Zhang CH, Jin F. Simulation of broadband seismic ground motions at dam canyons by using a deterministic numerical approach. Soil Dyn Earthq Eng 2015;76:136–44.
[12] Assimaki D, Gazetas G, Kausel E. Effects of local soil conditions on the topographic aggravation of seismic motion: parametric investigation and recorded field evidence from the 1999 Athens earthquake. Bull Seismol Soc Am 2005;95(3):1059–89.
[13] Assimaki D, Jeong S. Ground-motion observations at Hotel Montana during the M7.0 2010 Haiti earthquake: topography or soil amplification? Bull Seismol Soc Am 2013;103(5):2577–90.
[14] Mohammadi K, Asimaki D. Topography effects are not dominated by ground surface geometry: a site effects paradox. Geotech Front 2017:171–81.
[15] Lee SJ, Chan YC, Komatitsch D, Huang BS, Tromp J. Effects of realistic surface topography on seismic ground motion in the Yangminshan region of Taiwan based upon the spectral-element method and LiDAR DTM. Bull Seismol Soc Am 2009;99(2A):681–93.
[16] Wang L, Wu Z, Xia K. Effects of site conditions on earthquake ground motion and their applications in seismic design in loess region. J MT Sci 2017;14(6):1185–93.
[17] Arup. Final report on overall seismic hazard assessment. Landslip Prevention and Mitigation Programme, Pilot seismic microzonation study in North-West New Territories for the study of potential effect of earthquake on natural terrain investigation. Ove Arup & Partners Hong Kong Ltd.; 2012.
[18] Rai M, Rodriguez-Marek A, Yong A. An empirical model to predict topographic effects in strong ground motion using California small to medium magnitude earthquake database. Earthq Spectra 2016;32(2):1033–54.
[19] Rai M, Rodriguez-Marek A, Chiou BS. Empirical terrain-based topographic modification factors for use in ground motion prediction. Earthq Spectra 2017;33(1):157–77.
[20] Maufroy E, Cruz-Atienza VM, Cotton F, Gaffet S. Frequency-scaled curvature as a proxy for topographic site-effect amplification and ground-motion variability. Bull Seismol Soc Am 2015;105(1):354–67.
[21] Komatitsch D, Vilotte JP. The spectral element method: an efficient tool to simulate the seismic response of 2D and 3D geological structures. Bull Seismol Soc Am 1998;88(2):368–92.
[22] Komatitsch D, Tromp J. Introduction to the spectral element method for three-dimensional seismic wave propagation. Geophys J Int 1999;139(3):806–22.
[23] Savage B, Komatitsch D, Tromp J. Effects of 3D attenuation on seismic wave amplitude and phase measurements. Bull Seismol Soc Am 2010;100(3):1241–51.
[24] He CH, Wang JT, Zhang CH. Nonlinear Spectral-Element Method for 3D Seismic-Wave Propagation. Bull Seismol Soc Am 2016;106(3):1074–87.
[25] Wang G, Du C, Huang D. Topographic amplification of ground motions: a case study of Hong Kong. In: Proceeding of the 1st International Symposium on Soil Dynamics and Geotechnical Sustainability, August 7-9, Hong Kong; 2016.
[26] Lysmer J, Kuhlemeyer RL. Finite dynamic model for infinite media. J Eng Mech Div 1969;95(4):859–78.
[27] Wang G, Sitar N. Static and dynamic axial response of drilled piers. II: numerical evaluation. J Geotech Geoenviron Eng 2011;137(12):1143–53.
[28] Carcione JM. Wave fields in real media: wave propagation in anisotropic, anelastic, porous and electromagnetic media. Handbook of Geophysical Exploration: Seismic Exploration 38. Elsevier; 2007.
[29] Huang D, Wang G. Stochastic simulation of regionalized ground motions using wavelet packets and cokriging analysis. Earthq Eng Struct Dyn 2015;44:775–94.
[30] Huang D, Wang G. Region-specific spatial cross-correlation model for stochastic simulation of regionalized ground-motion time histories. Bull Seismol Soc Am 2015;105(1):272–84.
[31] Wang G, Youngs R, Power M, Li Z. Design ground motion library: an interactive tool for selecting earthquake ground motions. Earthq Spectra 2015;31(2):617–35.
[32] Huang D, Wang G. Energy-compatible and spectrum-compatible (ECSC) ground motion simulation using wavelet packets. Earthq Eng Struct Dyn 2017;46:1855–73.
[33] Du W, Wang G. A one-step Newmark displacement model for probabilistic seismic slope displacement hazard analysis. Eng Geol 2016;205:12–23.
[34] Du W, Huang D, Wang G. Quantification of model uncertainty and variability in Newmark displacement analysis. Soil Dyn Earthq Eng 2018;109:286–98.
[35] Du W, Wang G, Huang D. Evaluation of seismic slope displacements based on fully coupled sliding mass analysis and NGA-West2 database. J Geotech Geoenviron Eng 2018;144(8):06018006.